



AMERICAN METEOROLOGICAL SOCIETY

Journal of the Atmospheric Sciences

EARLY ONLINE RELEASE

This is a preliminary PDF of the author-produced manuscript that has been peer-reviewed and accepted for publication. Since it is being posted so soon after acceptance, it has not yet been copyedited, formatted, or processed by AMS Publications. This preliminary version of the manuscript may be downloaded, distributed, and cited, but please be aware that there will be visual differences and possibly some content differences between this version and the final published version.

The DOI for this manuscript is doi: 10.1175/JAS-D-16-0353.1

The final published version of this manuscript will replace the preliminary version at the above DOI once it is available.

If you would like to cite this EOR in a separate work, please use the following full citation:

Pauluis, O., and F. Zhang, 2017: Reconstruction of Thermodynamic Cycles in a High-Resolution Simulation of a Hurricane. *J. Atmos. Sci.* doi:10.1175/JAS-D-16-0353.1, in press.

© 2017 American Meteorological Society

ABSTRACT

4
5 The relationship between energy transport and kinetic energy generation in a hurricane is
6 analyzed. The hydrological cycle has a negative impact on the generation of kinetic energy.
7 First, in a precipitating atmosphere, mechanical work must also be expended in order to lift
8 water. Second, the injection of water vapor at low relative humidity and its removal through
9 condensation and precipitation reduces the ability of a thermodynamic cycle to generate
10 work. This reduction can be directly quantified in terms of the change in the Gibbs free
11 energy between the water added and removed.

12 A newly developed approach, namely the Mean Air Flow As Lagrangian Dynamics Ap-
13 proximation, is used to extract thermodynamic cycles from the standard output of a nu-
14 merical simulation of a hurricane. While convection in the outer rainbands is inefficient
15 at producing kinetic energy, the deepest overturning circulation associated with the rising
16 air within the eyewall is an efficient heat engine that produces about 70% as much kinetic
17 energy as a comparable Carnot cycle. This confirms that thermodynamic processes play a
18 central role in hurricane formation and intensification, and that the thermodynamic cycles in
19 a hurricane are characterized by high generation of kinetic energy which differ significantly
20 from those found in atmospheric convection.

21 1. Introduction

22 Intense winds in hurricanes and typhoons require a continuous generation of kinetic en-
23 ergy within the storm to balance frictional dissipation. The hurricane circulation transports
24 energy received from the warm ocean to the colder atmosphere. In doing so, it acts as a
25 heat engine that produces the kinetic energy necessary to sustain the storm. The ability to
26 generate kinetic energy can be quantified by an efficiency defined as the fraction of the heat
27 input that is converted into kinetic energy. The efficiency depends on multiple environmental
28 factors, such as the temperature of the energy source and sink, or the relative humidity of
29 the air. In this paper, we will review these factors and show how to assess the efficiency for
30 storms simulated in high resolution atmospheric models.

31 The Carnot cycle is probably the best known theoretical model for a heat engine. Its
32 efficiency is the maximum efficiency of any closed thermodynamic cycle and is equal to
33 the ratio of the temperature difference between the heat source and sink to the absolute
34 temperature of the heat source. Hurricanes have at times been compared to a Carnot cycle
35 (Emanuel 1986, 2003; Willoughby 1999) in which the energy source is the warm ocean surface
36 and the energy sink corresponds to the radiative cooling of the troposphere. For a typical
37 ocean temperature of about 300K and tropopause temperature of 200K, hurricanes would
38 be able to convert up to one third of the energy input into kinetic energy.

39 However, not all heat engines act as Carnot cycle. There is a growing body of evidence
40 that the hydrological cycle leads to a substantial reduction of the generation of kinetic
41 energy by the Earth's atmosphere. This occurs for two reasons. First, a substantial fraction
42 of the work done by the atmosphere is used to lift water and is subsequently dissipated as
43 precipitation falls to the ground (Pauluis et al. 2000; Pauluis and Dias 2013). Second, the
44 atmosphere acts as a dehumidifier that gains water through evaporation in unsaturated air
45 but loses it as liquid water. This corresponds to a thermodynamic transformation in which
46 the reactant (water vapor) has a lower Gibbs free energy state than the product (liquid
47 water or ice). Such reaction cannot occur spontaneously in an isolated system and reduces

48 the ability of the system to generate mechanical work (Pauluis 2011). Several studies (Pauluis
49 and Held 2002a; Laliberte et al. 2015; Pauluis 2016) have confirmed the negative impacts of
50 the hydrological cycle on the atmospheric heat engine efficiency at both the convective and
51 global scales.

52 This raises the questions of whether hurricanes can generate kinetic energy at a rate
53 expected from a Carnot cycle, and, if so, of why hurricanes would be less affected by moist
54 processes than other atmospheric motions. To address this issue, we will analyze the thermo-
55 dynamic behavior of an idealized hurricane simulation. Computing the mechanical output
56 of a thermodynamic cycle is straightforward for idealized cycles. This task is more difficult
57 for highly turbulent flows in which the trajectories of air parcels vary greatly and are not
58 periodic. To address this problem here, we use a new analytical framework, the "Mean Air
59 Flow As Lagrangian Dynamics Approximation" (MAFALDA hereafter, see Pauluis 2016).
60 Under MAFALDA, one first computes the overturning circulation in isentropic coordinates
61 by sorting rising and descending air parcels in terms of their equivalent potential tempera-
62 ture. This mean circulation is then used to construct a set of thermodynamic cycles with the
63 same mass and heat transport as the total flow. The thermodynamic transformations along
64 these cycles are then analyzed to assess the impacts of moist processes on kinetic energy
65 generation in the hurricane.

66 Section 2 reviews the impacts of the hydrological cycle on the kinetic energy generation
67 in a generic thermodynamic cycle with condensation and precipitation. It shows that the
68 mechanical output of such a cycle is reduced by a Gibbs penalty term that accounts for
69 the addition and removal of water substance in different thermodynamic states. Section
70 3 describes the MAFALDA procedure and applies it to a hurricane simulation. Section
71 4 analyzes the thermodynamic cycles in our simulation to show that the thermodynamic
72 cycle associated with ascent within eyewall can achieve an efficiency comparable to that of
73 a Carnot cycle. Our results are summarized in Section 5.

2. Impacts of the hydrological cycle on the atmospheric heat engine.

We consider a schematic representation of the overturning circulation in a hurricane as presented in Figure 1. As air rushes toward the center of the storm (point 1 \rightarrow 2), it gains energy and entropy due to the energy flux from the surface. It then ascends in the eyewall, undergoing a near adiabatic expansion, and moves away from the storm center in the upper troposphere (point 2 \rightarrow 3). The air is eventually brought back to the surface while losing energy through the emission of infrared radiation (point 3 \rightarrow 1). These transformations correspond to a heat engine which transports energy from the ocean surface to the upper troposphere and is associated with a net conversion of internal energy into kinetic energy.

Quantitatively, we define the efficiency of a heat engine η as the ratio of the generation of kinetic energy W_{KE} to the external heating Q_{in} :

$$\eta = \frac{W_{KE}}{Q_{in}} \quad (1)$$

The potential intensity theory of Emanuel (1986) indicates that a hurricane acts in similar fashion to a Carnot cycle. In particular, the efficiency is equal to the well-known Carnot efficiency η_C :

$$\eta_C = \frac{T_{in} - T_{out}}{T_{in}} \quad (2)$$

where T_{in} and T_{out} are respectively the temperatures of the energy source and sink.

While the total work and heat flux is proportional to the mass of air being circulated, the efficiency is not. Here, we compute the energy flux and mechanical work per unit mass of dry air circulated. The external heating δq can be directly assessed from the First Law of Thermodynamics by:

$$\delta q = dh - \alpha_d dp. \quad (3)$$

Here, h is the enthalpy per unit mass of dry air, α_d is the specific volume per unit mass of dry air, and p is the total pressure. The external heating here should be understood as

external with respect to the parcel. It not only includes energy exchange with the surface and radiative cooling, but also diffusive energy transfer and frictional heating. The net energy source Q_{in} and net energy sink Q_{out} are defined as the integral of the positive and negative values of δ_q along the cycle. Integrating 3 over a cycle, yields

$$Q_{in} + Q_{out} = W_{KE} + W_P. \quad (4)$$

The left-hand side here is equal to the net heating, while the right-hand side is equal to the total amount of work produced. The later is separated into the generation of kinetic energy W_{KE}

$$W_{KE} = - \oint \alpha_d dp - \oint \Gamma(r_v + r_i + r_l) dz. \quad (5)$$

and the work done to lift water

$$W_P = \oint \Gamma(r_v + r_i + r_l) dz. \quad (6)$$

Here, Γ is the gravitational acceleration, and r_v , r_l and r_i are respectively the mass of water vapor, liquid water and ice per unit mass of dry air.

To relate the generation of work to the energy transport, we can take advantage of the Gibbs relationship (see equation A.6) to rewrite the external heating (3) as

$$\delta q = T ds + \sum_{w=v,l,i} g_w dr_w. \quad (7)$$

Here, s is the moist entropy per unit mass of dry air, T is the temperature, and g_v , g_l and g_i are the specific Gibbs free energy for water vapor, liquid water and ice. The Gibbs free energy terms are necessary here to fully account for the thermodynamic impacts associated with the addition and removal of water in different phases. These quantities are defined in the Appendix. Dividing equation (7) by the absolute temperature and integrating over a thermodynamic cycle yields

$$\frac{Q_{in}}{T_{in}} + \frac{Q_{out}}{T_{out}} + \frac{\Delta G}{T_{out}} = 0. \quad (8)$$

We refer here to the term ΔG as the Gibbs penalty and it is defined as

$$\Delta G = -T_{out} \oint \sum_{w=v,l,i} \frac{g_w}{T} dr_w. \quad (9)$$

115 Equations (4) and (8) can be combined to yield an expression for the generation of kinetic
116 energy:

$$W_{KE} = \frac{T_{in} - T_{out}}{T_{in}} Q_{in} - W_P - \Delta G. \quad (10)$$

117 The first term on the right-hand side is the work that would have been produced by a Carnot
118 cycle. The generation of kinetic energy is less than this theoretical maximum due to the work
119 necessary to lift the water W_P and due to the thermodynamic impact of the hydrological
120 cycle quantified in terms of the Gibbs penalty ΔG .

121 In the idealized cycle, water vapor is added as unsaturated water vapor and removed
122 mostly as liquid water or ice. The Gibbs free energy of unsaturated water vapor is always
123 less than that of liquid water at the same temperature with $g_v - g_l = R_v T \ln \mathcal{H}$, where R_v
124 is the specific gas constant for water vapor and \mathcal{H} is the relative humidity. This implies
125 that water is added to the cycle at a lower Gibbs free energy than it is removed, thus
126 corresponding to a positive value of the Gibbs penalty and a reduction of the mechanical
127 output.

128 A physical process, such as condensation of unsaturated water vapor, in which the Gibbs
129 free energy of the products is higher than that of the reactants cannot occur under isothermal
130 and isobaric condition, as it would imply a violation of the Second Law of Thermodynam-
131 ics. Indeed, in such situation, the reverse reaction, e.g. the evaporation of liquid water
132 in unsaturated air, occurs spontaneously. As the transformations involved in the idealized
133 hurricane cycle described in Figure 1 are neither isothermal nor isobaric, they can result in a
134 net increase in the Gibbs free energy without violating the Second Law. However, equation
135 (10) indicates that, when this happens, the cycle must be associated with a heat transport
136 from warm to cold, and the mechanical output is reduced by an amount equal to the Gibbs
137 penalty.

138 The difference of Gibbs free energy between water vapor and liquid water, $g_v - g_l =$
139 $R_v T \ln \mathcal{H}$, is equal to the amount of work that could be produced by the isothermal expan-
140 sion of water vapor from its saturation partial pressure to its actual partial pressure. And

141 indeed, this is equal to the amount of work that is produced if water vapor first evaporates in
142 saturated condition then expands to reach the partial pressure in the environment. However,
143 when evaporation occurs in unsaturated air, water molecules irreversibly diffuse into unsatu-
144 rated air, without generating any mechanical work. Instead, there is an irreversible increase
145 of entropy equal to the increase of Gibbs free energy divided by the absolute temperature.
146 Thus, the Gibbs penalty can be thought of as the amount of work that the thermodynamic
147 cycle fails to produce due to the thermodynamic irreversibility tied to the hydrological cycle.

148 **3. Reconstruction of thermodynamic cycles from nu-** 149 **merical simulations**

150 *a. Numerical model and set-up*

151 We analyze here the thermodynamic behavior of a hurricane simulated with the Advanced
152 Research version of the Weather Research and Forecasting (WRF-ARW) model version 3.1.1
153 Skamarock et al. (2008). In this configuration, the model uses three two-way nested domains,
154 with respective sizes of 4320 km by 4320 km, 1440 km by 1440 km, and 720 km by 720 km,
155 and with horizontal grid spacings of 18, 6, and 2 km. The model has 41 vertical levels with
156 the model top at 50 hPa. The two smaller nested domains are moveable, with the domain
157 center following the 850-hPa center of the tropical cyclones. The physical parameterizations
158 are the same as in Zhang and Tao (2013) and Tao and Zhang (2014). It should be noted
159 that the turbulent parameterization used in WRF does not include a frictional heating, i.e.
160 the kinetic energy loss to dissipation is not put back as internal energy. Bister and Emanuel
161 (1998) have suggested that the inclusion of frictional heating can lead to more intense tropical
162 storms. The model is initialized with a modified Rankine vortex with a maximum surface
163 wind speed of 15 ms^{-1} at 135 km radius. The Dunion non-SAL mean hurricane season
164 sounding (Dunion 2011) is used for the environmental moisture and temperature profile

165 with a constant sea surface temperature of 29°C (SST29) and a constant Coriolis parameter
166 equivalent to 20N. The initial condition and model setup are the same as the noflow-SST29
167 in Tao and Zhang (2014) but without moisture perturbation.

168 Figure 2 shows the evolution of the maximum wind and minimum pressure. The hurricane
169 reaches its maximum intensity by the end of day 5, with a central pressure of 885 mb and
170 a maximum wind speed of 97 ms⁻¹. The storm maintains its intensity for the remaining 10
171 days of simulation, with a slight increase in surface pressure by day 15. As the experimental
172 set-up used here does not include radiative transfer, the atmosphere will slowly evolve toward
173 a state of a thermal equilibrium with the ocean, with no convection or wind. Over the
174 course of the simulation, we observe an increase in low level humidity away from the storm,
175 a warming of the upper-troposphere, and a reduction of the convective activity far away from
176 the storm center. All these are consistent with a slow evolution toward thermal equilibrium.
177 The storm however occupies only a small fraction of the domain and, as noted earlier, its
178 intensity remains steady for the last 10 days of the simulation. Our main focus here is
179 to analyze the thermodynamic cycles that underlie the storm, and we chose here to focus
180 primarily on the intensifying storm on day 5 of the simulation.

181 Figures 3A shows the mean azimuthal wind during the fifth day of the simulation. It
182 exhibits a well defined maximum near the surface at a radius of about 40 km from the storm
183 center. The strong vortex extends through the entire troposphere. Further away from the
184 center, in the upper troposphere, the circulation is anticyclonic, as evidenced by the negative
185 azimuthal wind.

186 Figure 3B shows the distribution of equivalent potential temperature θ_e . The equivalent
187 potential temperature here is defined with respect to ice, as in Pauluis (2016). The definition
188 of θ_e used here includes a contribution from the latent heat of freezing, and is slightly higher
189 than the equivalent potential temperature over liquid water as defined in Emanuel (1994).
190 Away from the center of the storm, the equivalent potential temperature shows a vertical
191 structure typical of the tropical regions, with high value near the surface, $\theta_e \approx 360\text{K}$, a lower

192 tropospheric minimum with $\theta_e \approx 335\text{K}$ at an altitude of 4-5km, then a slow increase in the
 193 upper troposphere. The stratosphere is not shown in Figure 3B but it exhibits an enhanced
 194 stratification. Toward the center of the storm, the equivalent potential temperature increases
 195 and the midtropospheric minimum of θ_e becomes less pronounced. The eyewall appears as
 196 a region of almost constant value of θ_e .

197 The secondary circulation can be quantified in terms of an Eulerian streamfunction

$$\Psi_E(r, z) = \int_0^r \rho w r dr, \quad (11)$$

198 which is shown in Figure 3C. The streamfunction shows a direct overturning circulation,
 199 with inflow at low level, rising motion in the eyewall and outflow in the upper troposphere.
 200 Figure 3C also indicates another inflow in the upper troposphere located between 10 and
 201 12km, below the main outflow. Similar upper level inflows have been noted in other numerical
 202 simulations of hurricanes, such as Rotunno and Emanuel (1987).

203 *b. The Mean Air Flow As Lagrangian Dynamics Approximation*

204 The analysis of the thermodynamic cycles in the previous section requires us to know
 205 the evolution of the thermodynamic properties of an air parcel. Most atmospheric flows are
 206 highly turbulent, and not only are all parcel trajectories different, but they almost never
 207 correspond to a closed thermodynamic cycle. To circumvent this problem, Pauluis (2016)
 208 introduced MAFALDA, a systematic approach designed to extract a set of representative
 209 cycles from numerical simulations of turbulent atmospheric flows. The method consists of 4
 210 distinct steps:

- 211 i. Compute the isentropic streamfunction in $z - \theta_e$ coordinates;
- 212 ii. Estimate the conditional average of thermodynamic state variables as function of z
 213 and θ_e ;
- 214 iii. Construct a set of trajectories in $z - \theta_e$ from the isentropic streamfunction;

215 iv. Interpolate the values of the various state variables along these trajectories;

216 1) ISENTROPIC STREAMFUNCTION

217 Under MAFALDA, one first computes a mean overturning circulation using height (z)
218 and equivalent potential temperature θ_e as coordinates. It is quantified in terms of the
219 isentropic streamfunction $\Psi(z, \theta_e)$ shown in Figure 4, defined as the net upward mass flux
220 at height z of all air parcels with an equivalent potential temperature less than θ_{e0} :

$$\Psi(z, \theta_{e0}) = \frac{1}{P} \int_{t_0}^{t_0+P} \int_0^{2\pi} \int_0^{r_0} \rho(w - \bar{w})H(\theta_{e0} - \theta_e(r, \phi, z, t)) r dr d\phi dt. \quad (12)$$

221 Here, $P = 1$ day is the time period for the averaging, $r_0 = 800$ km is the radius of the domain
222 used for averaging, ρ is the mass of dry air per unit volume, w is the vertical velocity, $\bar{w}(r, z)$ is
223 the mass weighted horizontally averaged velocity for $r < r_0$ and H is the Heaviside function.
224 Note that the integral in (12) is computed only for a central part of the simulated domain.
225 Convection far away for the storm center dominates the isentropic streamfunction when it
226 is computed over the entire domain, making the thermodynamic structure of the hurricane
227 more difficult to distinguish. We choose here to limit the isentropic analysis to an area
228 relatively close to the storm instead. The isentropic streamfunction is introduced in Pauluis
229 and Mrowiec (2013) and its application to hurricanes is discussed in Mrowiec et al. (2016).

230 The isentropic streamfunction averaged over the 5th day of the simulation is shown in
231 Figure 4. For a steady flow, the mean flow in $z - \theta_e$ coordinates follows the isolines of the
232 streamfunction. In Figure 4, this flow would be clockwise, with air rising at high value of θ_e
233 near the center of the storm and subsiding at lower θ_e much further away. The ascent in the
234 eyewall corresponds to rising motions at very high value of θ_e , here for $365K < \theta_e < 380K$.
235 The ascent of high θ_e air in the eyewall accounts for only one third of the total the overturning,
236 with the bulk of the ascent occurring at lower value of θ_e , with $355K < \theta_e < 365K$.

237 There are substantial differences between the overturning identified by the Eulerian
238 and isentropic streamfunctions depicted respectively in Figure 3C and Figure 4. Notably,

239 the mass transport is much larger in the isentropic analysis, with a maximum value of
 240 about $1.4 \cdot 10^{10} \text{kg s}^{-1}$, than in the Eulerian frame, which has a maximum value of about
 241 $0.6 \cdot 10^{10} \text{kg s}^{-1}$. The maximum of the isentropic streamfunction is also located near the sur-
 242 face, while the Eulerian streamfunction peaks in the upper troposphere. In addition, the
 243 isentropic analysis indicates that rising air parcels exhibit high value of θ_e , with $\theta_e > 355 \text{K}$,
 244 which is substantially larger than the value of θ_e found in the free troposphere away from the
 245 boundary layer and eyewall. These differences can be attributed to the mass transport by
 246 convective motions, which is not accounted for by the Eulerian averaging. We will refer the
 247 interested readers to Mrowiec et al. (2016) for a more detailed discussion of the difference
 248 between isentropic and Eulerian circulations in hurricanes.

249 2) MAFALDA TRAJECTORIES:

250 In MAFALDA, the isolines of the isentropic streamfunction are treated as parcel trajec-
 251 tories. For a given value of the streamfunction Ψ_0 , we construct a parametric representation
 252 $(z(\lambda), \theta_e(\lambda))$ of the isoline such that

$$\Psi(z(\lambda), \theta_e(\lambda)) = \Psi_0. \quad (13)$$

253 We focus here on two distinct cycles corresponding to 2.5% and 42.5% of the absolute
 254 minimum of the streamfunction. Three locations are marked along each cycle: point 1 is the
 255 minimum entropy, point 2 corresponds to the maximum entropy at the surface, and point 3
 256 is the highest point in the cycle.

257 The first trajectory, indicated by the solid black line, is referred here to as the inner-core
 258 cycle, and is associated with air parcels rising at very high equivalent potential temperature,
 259 with $\theta_e \approx 370 \text{K}$. The second trajectory, which we will refer to as the rainband cycle, is
 260 representative of air parcels that rise at lower value of the equivalent potential temperature,
 261 with $\theta_e \approx 350 \text{K}$ in the upper troposphere. These two trajectories are shown respectively
 262 as the solid black line and the blue dashed lines in Figures 3A-C. To convert a trajectory

263 in isentropic coordinates $\theta_e - z$, to the Eulerian coordinates $r - z$, we compute the mean
 264 radius associated with air parcels at a given value of z and θ_e as discussed in the next
 265 subsection. Figure 3A shows that the inner-core cycle indeed corresponds to an air parcel
 266 that penetrates to near the center of the storm, rises to the tropopause within the eyewall
 267 before moving outward and subsiding far away from the center. In contrast, the rainband
 268 cycle is associated with rising motion further away from the center, in the region associated
 269 with the outer rainbands of the storms.

270 3) ISENTROPIC AVERAGE OF STATE VARIABLES

271 To evaluate the value of the various properties of the air parcels along the streamlines,
 272 we compute their mass-weighted conditionally averaged value in $z - \theta_e$ coordinates. First,
 273 for any function $f(x, y, z, t)$, we introduce its isentropic integral $\langle f \rangle$ as

$$\langle f \rangle (z, \theta_{e0}) = \frac{1}{P} \int_{t_0}^{t_0+P} \int_0^{2\pi} \int_0^{r_0} f \delta(\theta_{e0} - \theta_e(r, \phi, z, t)) r dr d\phi dt,$$

274 where δ is the Dirac delta function. The mass-weighted average of f is defined as

$$\tilde{f}(z, \theta_{e0}) = \frac{\langle \rho f \rangle}{\langle \rho \rangle}.$$

275 Figure 5 shows the isentropic average for the radius \tilde{r} , azimuthal wind, specific moist
 276 entropy \tilde{s} , temperature \tilde{T} , mixing ratio \tilde{r} and Gibbs free energy \tilde{g}_v , respectively. The radius
 277 distribution in Figure 5A shows that air with high θ_e is preferentially located near the
 278 storm center, while low energy air parcels, with θ_e less than 345K, are located far away
 279 from the center, with $\tilde{r} \geq 500\text{km}$. At low levels, the radius \tilde{r} decreases with increasing
 280 θ_e , corresponding to the gradual moistening of the air toward the center of the storm. The
 281 azimuthal wind \tilde{u} is shown in Figure 5B. The strongest wind corresponds to the air with high
 282 θ_e near the surface. A benefit of the isentropic averaging here is to magnify the structure of
 283 the eyewall. Indeed, while the eyewall occupies a small physical area near the storm center,
 284 it is associated with a fairly broad range of high values of θ_e between 355K and 375K.

285 Figures 5C and 5D show the distribution of moist entropy \tilde{s} and temperature \tilde{T} . There is
 286 a close relationship between equivalent potential temperature and entropy, which translates
 287 in that the isolines for \tilde{s} are almost vertical. Similarly, the isolines for temperature \tilde{T} are
 288 almost horizontal, as the the temperature variations are closely tied to changes in height.
 289 The water vapor distribution (Figure 5E) shows high value near the surface and at high
 290 equivalent potential temperature. The decreases of water vapor with height is due to the
 291 decrease in temperature through the Clausius Clapeyron relationship. At a given height,
 292 fluctuations of water vapor are strongly linked to the horizontal variations of equivalent
 293 potential temperature. Figure 5F shows the distribution of the Gibbs free energy of water
 294 vapor g_v . The variations of g_v are foremost determined by relative humidity. At high value of
 295 θ_e , g_v is close to 0, indicating that these air parcels are saturated with respect to liquid water.
 296 Lower values of θ_e are associated with large negative value of g_v in the unsaturated storm
 297 environment. In the upper troposphere, the Gibbs free energy is negative as condensation
 298 over ice reduces the water vapor pressure well below its saturation value over liquid water.

299 4) STATE VARIABLES ALONG THE MAFALDA TRAJECTORIES:

300 State variables along given MAFALDA trajectories are taken to be equal to the corre-
 301 sponding isentropic average at the same value of z and θ_e , e.g.:

$$s(\lambda) = \tilde{s}(z(\lambda), \theta_e(\lambda)).$$

302 This procedure allows us to estimate the value of any state variable along any of the
 303 MAFALDA trajectories. The solid black line and the dashed blue line on Figure 5 show
 304 the MAFALDA trajectories associated with the cycles superimposed on the isentropic aver-
 305 age for various state variables.

306 We apply the MAFALDA procedure to reconstruct the thermodynamic cycles during
 307 the 5th day of our simulation. Figure 6 shows the results for the inner-core cycle and the
 308 rainband cycles under six different coordinate pairs: moist entropy (s) and temperature (T)

309 (Figure 6A); buoyancy b and height z (Figure 6B); total water content $r_T = r_v + r_l + r_i$
 310 and height z (Figure 6C); mixing ratio q and Gibbs free energy for water vapor g_v (Figure
 311 6D); liquid water content r_l and Gibbs free energy for liquid water g_l (Figure 6E); and ice
 312 water content q_i and Gibbs free energy for ice g_i (Figure 6F). The axes are chosen so that
 313 the trajectories are going clockwise in all four panels, with x and y directions corresponding
 314 qualitatively to increasing radius and increasing height. Three locations are marked along
 315 each cycles: point 1 is the entropy minimum, point 2 corresponds to the maximum entropy
 316 at the surface, and point 3 is the highest point in the cycle.

317 4. Thermodynamic cycles in a simulated hurricane

318 The MAFALDA procedure has allowed us to extract thermodynamic cycles from the
 319 numerical model output. We now turn to the physical interpretation of the cycles in various
 320 thermodynamic coordinates as shown in Figure 6, and their implications for the generation
 321 of kinetic energy.

322 In the T-S diagram (Figure 6A), the two trajectories exhibit features of a heat engine.
 323 For the inner-core cycle, the first transformation from 1 to 2 leads to an entropy increase
 324 from $200JK^{-1}kg^{-1}$ to $300JK^{-1}kg^{-1}$ due to the energy fluxes from the ocean surface. The
 325 second transformation from 2 to 3 corresponds to an expansion with approximately constant
 326 moist entropy but decreasing temperature from 300K to about 200K. In the last leg from
 327 3 to 1, the parcel is compressed back to the surface and its temperature increases from
 328 200K to about 300K. As first, the parcel loses energy and its entropy decreases from about
 329 $300JK^{-1}kg^{-1}$ to $200JK^{-1}kg^{-1}$. Closer to the surface, water vapor gained from mixing with
 330 cloudy air leads to an entropy increase from $200JK^{-1}kg^{-1}$ to $240JK^{-1}kg^{-1}$.

331 The rainband cycle differs from the inner-core cycle in three aspects. First, the entropy
 332 increase in the inflow portion of the cycle ($1 \rightarrow 2$) is substantially less for the rainband cycle
 333 indicative of weaker surface energy fluxes. Second, the entropy decreases from about 280 to

334 $250JK^{-1}$ during the ascent ($2 \rightarrow 3$). This loss of entropy occurs as the air parcel loses water
 335 vapor through detrainment and mixing: a reduction of entropy of $30JK^{-1}kg^{-1}$ corresponds
 336 approximately to a loss of $3g/kg$ of water vapor. Finally, the rainband cycle is shallower,
 337 reaching a height of 12km and its minimum temperature (at about 220K) is substantially
 338 warmer than for the inner-core cycle.

339 Figure 6B shows the two cycles in buoyancy and height coordinates. The buoyancy here
 340 is given by

$$b = \Gamma \left(\frac{T - \bar{T}}{\bar{T}} + \frac{R_v}{R_d}(r_v - \bar{r}_v) - (r_T - \bar{r}_T) \right),$$

341 where the overbar denotes the horizontal average. In an anelastic model, the generation of
 342 kinetic energy would be proportional to the integral of $\oint b dz$, i.e. the area within the curve
 343 shown in Figure 6B. As the Mach number in a hurricane is high, the anelastic approximation
 344 is inaccurate, and the generation of kinetic energy should be computed by the integral (10).
 345 Nevertheless, we use here the buoyancy-height coordinates as it makes it easier to visualize
 346 the cycles. In both cycles, rising air is lighter than descending air, so that the cycles are
 347 associated with a net generation of kinetic energy. The variations of buoyancy in the inner-
 348 core cycle are particularly large - reaching up to $0.4ms^{-2}$. The kinetic energy generation
 349 is approximately equal to the area within the curve, and Figure 6B thus indicates that the
 350 inner-core cycle generates much more kinetic energy than the rainband cycle.

351 Figure 6C shows the two cycles in total water mixing ratio and height coordinates. Both
 352 cycles corresponds to a net upward transport of water in all phases. The geopotential energy
 353 gained by the water as it is lifted by atmospheric motions, is proportional to the area within
 354 the cycle. The inner-core cycle does more work in order to lift more water to a higher level
 355 than the rainband cycle. The maximum mixing ratio in the inner-core cycle is about 22
 356 g/kg, which is about 2g/kg larger than for the outer rainband cycle. This is consistent
 357 with the difference of about $20JK^{-1}kg^{-1}$ in the maximum entropy between the two cycles,
 358 and confirms that the entropy increase near the center of the storm is due to the enhanced
 359 evaporation from the ocean.

360 These cycles differ from a Carnot cycle in a more fundamental way: most of the entropy
361 increase arises from the evaporation of water at the ocean surface. The air parcel must
362 be treated as an open system that exchanges water in various phases. Figure 6D shows
363 the two cycles in $r_v - g_v$ coordinates with clockwise trajectories. The Gibbs free energy of
364 water vapor can be approximated as $g_v \approx R_v T \ln \mathcal{H}$ and its variations depends primarily on
365 relative humidity. Surface evaporation $1 \rightarrow 2$ also corresponds to a gain of water vapor at
366 low value of the Gibbs free energy. Expansion $2 \rightarrow 3$ corresponds to a loss of water vapor
367 through condensation and precipitation. As the air is saturated through the expansions,
368 the Gibbs energy of the water vapor closely matches that of liquid water below the freezing
369 level, and that of ice above it. During compression $3 \rightarrow 1$, the air parcel gradually gains
370 water vapor from mixing with surrounding clouds. Water is injected into unsaturated air at
371 a low value of the Gibbs free energy ($1 \rightarrow 2$ and $3 \rightarrow 1$) but removed during the expansion
372 as condensed water with higher Gibbs free energy ($2 \rightarrow 3$). From a thermodynamic point
373 of view, a chemical reaction where the reactant, water vapor, has a lower Gibbs free energy
374 than the product, liquid water, does not occur spontaneously under isothermal conditions.
375 The hydrological cycle is possible here because evaporation occurs systematically at higher
376 temperature than condensation. The difference in Gibbs free energy between evaporation
377 and condensation also leads to a reduction of the kinetic energy generated by the atmospheric
378 heat engine.

379 Figures 6E and 6F show the two cycles in the mixing ratio and Gibbs free energy for
380 liquid water ($g_l - r_l$ in Figure 6E) and ice ($g_i - r_i$ in Figure 6F). These are necessary for the
381 computation of the Gibbs penalty ΔG , but the contribution of the water and ice phase is
382 quite smaller than the contribution from water vapor, due to the facts that there is much less
383 liquid water and ice present, and that the variations of Gibbs free energy for water are small
384 when compared to that of water vapor. The decision here to use liquid water at $273.15K$ as
385 the reference state ensures that the Gibbs free energy of water is small and slightly negative.

386 We apply the thermodynamic framework of section 2 to analyze the kinetic energy gen-

387 eration in each thermodynamic cycle computed from MAFALDA. The energy source Q_{in}
 388 and sink Q_{out} are computed by integrating the positive and negative values of the heating
 389 increment $\delta q = dh - \alpha_d dp$:

$$Q_{in} = \oint \max(\delta q, 0) \quad (14)$$

$$Q_{out} = \oint \min(\delta q, 0) \quad (15)$$

390 The temperature of the energy source T_{in} and sink T_{out} are obtained by

$$\frac{Q_{in}}{T_{in}} = \oint \max\left(\frac{\delta q}{T}, 0\right) \quad (16)$$

$$\frac{Q_{out}}{T_{out}} = \oint \min\left(\frac{\delta q}{T}, 0\right). \quad (17)$$

391 The Carnot efficiency η_C is equal to the temperature difference between the energy source
 392 and energy sink, divided by the temperature of the energy source

$$\eta_C = \frac{T_{in} - T_{out}}{T_{in}}, \quad (18)$$

393 so that the maximum work that could be achieved by an equivalent Carnot cycle W_{max} is
 394 equal to the product of the net heating multiplied by the Carnot efficiency $W_{max} = \eta_C Q_{in}$.
 395 The generation of kinetic energy W_{KE} is given by equation (5), the work done to lift water
 396 W_P by equation (6) and the Gibbs penalty by equation (9). These quantities are related to
 397 each other in terms of the thermodynamic budget (10):

$$W_{KE} = W_{max} - W_P - \Delta G.$$

398 Note that all the values for the energy flux and work - $Q_{in}, Q_{out}, W_{max}, W_P, \Delta G$ and W_{KE}
 399 - are expressed in Joules per unit mass of dry air.

400 For the rainband cycle, our analysis yields an external heating $Q_{in} = 19.9 \text{ kJkg}^{-1}$ occurring
 401 at an average temperature $T_{in} = 294K$, while the cooling temperature is $T_{out} = 269K$.
 402 The Carnot efficiency for this cycle is $\eta_C = 0.08$, which corresponds to a maximum work
 403 $W_{max} = \eta_C Q_{in} = 1.68 \text{ kJkg}^{-1}$. The generation of kinetic energy $W_{KE} = 0.73 \text{ kJkg}^{-1}$ which

404 corresponds to a heat engine efficiency $\eta = W_{KE}/Q_{in} = 0.04$. This small efficiency is
 405 due both to the fact that a substantial portion of the work is used to lift water, with
 406 $W_P = 0.42 \text{ kJkg}^{-1}$, and to counter the Gibbs penalty $\Delta G = 0.48 \text{ kJkg}^{-1}$ resulting from
 407 the hydrological cycle. These numbers are similar to the ones obtained for the deepest
 408 MAFALDA cycle in moist convection (Pauluis 2016), which confirms that the rainband
 409 cycle is in a similar thermodynamic regime as deep convection in the tropics.

410 In contrast, the inner-core cycle is associated with a larger energy transport, with a net
 411 heating of $Q_{in} = 33.6 \text{ kJkg}^{-1}$. The temperature of the heat source is marginally lower than
 412 for the rainband cycle, with $T_{in} = 283\text{K}$. However, the temperature of the energy sink
 413 drops significantly to $T_{out} = 233\text{K}$. As the cycle acts on a larger temperature difference, its
 414 Carnot efficiency increases to $\eta_C = 0.18$. This larger Carnot efficiency combined with a larger
 415 energy transport leads to a large increase of the maximum work to $W_{max} = 5.91 \text{ kJkg}^{-1}$.
 416 The negative contributions from water lifting $W_P = 0.87 \text{ kJkg}^{-1}$ and Gibbs penalty $\Delta G =$
 417 0.76 kJkg^{-1} increase as well, but not at the same rate as the maximum work. The kinetic
 418 energy generation $W_{KE} = 4.18 \text{ kJkg}^{-1}$ is less than the theoretical maximum and corresponds
 419 to a heat engine efficiency $\eta = 0.13$ for the inner-core cycle.

420 Our analysis indicates that a striking six-fold increase in kinetic energy generation be-
 421 tween the rainband cycle and the inner-core cycle is due to a combination of three changes:
 422 (1) a 60% increase in the external heating associated with the intense evaporation at the
 423 center of the storm, (2) a substantial decrease in the cooling temperature (from 269K to
 424 233K) which results in a doubling of the the Carnot efficiency, and (3) the actual efficiency
 425 of the cycle becomes close to its Carnot efficiency. This later point can be attributed to the
 426 fact that relative increases in water lifting W_P and in Gibbs penalty ΔG are much weaker
 427 than the relative increase in W_{max} . As a result, while the heat engine efficiency of the rain-
 428 band cycle was only about 40% of the corresponding Carnot efficiency η_C , the inner- core
 429 cycle achieves about 70% of its Carnot efficiency.

430 The increase in surface heating between the rainband and inner-core cycles is a con-

431 sequence of the enhanced surface evaporation near the storm center, which has long been
432 recognized as one of the key requirements for the maintenance of hurricane. Enhanced evap-
433 oration by itself may not be sufficient however. Indeed, the maximum intensity theory of
434 Emanuel (1986) shows that the maximum wind depends not on entropy itself, but on the
435 entropy gradient near the storm center. To be effective, surface evaporation must lead to a
436 local increase in the moist entropy. The ratio Q_{in}/T_{in} is the amount of entropy that a parcel
437 gains from the energy source. In our simulation, the high value of Q_{in} for the inner-core cycle
438 is tied to the fact that the air parcels rising within the eyewall have an equivalent potential
439 temperature - about 370K - that is substantially larger than that of the environment.

440 The reduction of cooling temperature T_{out} from 269K to 233K between the rainband and
441 inner-core cycles leads to a substantial increase in the Carnot efficiency. The reduction in
442 cooling temperature can be partially attributed to the deepening of the cycle, as the inner-
443 core cycle reaches a height of 15km instead of 13km for the rainband cycle. However, this
444 fact does not by itself explain the large drop in T_{out} . Indeed, a closer look at the $s - T$
445 diagram for both cycles in Figure 6A reveals that the lowest temperature in rainband cycle
446 is about 220K which is not much different than the minimum temperature in the inner-core
447 cycle - about 200K. The cooling temperature T_{out} corresponds to the (harmonic) average
448 temperature at which the parcel loses energy. In the rainband cycle, there is a very clear loss
449 of entropy - and energy - during the ascent $2 \rightarrow 3$ due to the entrainment of dry air in the
450 convective updrafts. This energy loss occurs at warm temperature, between 275K and 300K
451 and shift the cooling temperature toward higher values. In contrast, the ascent in the inner-
452 core cycle is almost adiabatic, and most of the entropy loss occurs during the subsidence at
453 low temperature. Thus, the low cooling temperature and high Carnot efficiency in the inner-
454 core cycle require not only a deep overturning - so that cooling can occur at low temperature
455 - but also a lack of entrainment during the ascent - which would otherwise correspond to an
456 energy loss at relatively warm temperature.

457 Finally, the high generation rate of kinetic energy in the inner-core cycle is due in part to

458 the fact that this cycle is able to achieve an efficiency that is close to the Carnot efficiency.
459 While both the Gibbs penalty ΔG and the water loading W_P nearly double between the
460 rainband and the inner-core cycles, the maximum work W_{max} more than triples. Pauluis
461 (2016) argue that the Gibbs penalty and water loading depends primarily on how much
462 water is added and removed through a thermodynamic cycle, and are only weakly sensitive
463 to the depth of the cycle. As such, deep thermodynamic cycles are less hindered by moist
464 processes and their efficiency is closer to their Carnot efficiency.

465 We further analyze 20 cycles from MAFALDA, ordered from the deepest inner-core cycle
466 1 to the shallowest cycle 20, with the rainband cycle described above corresponding to cycle
467 8. The cycles are constructed from different values of the stream function and are ordered
468 from the deepest to the shallowest. Figure 7A shows the four terms from equation (10).
469 Deep cycles transport more energy across a larger temperature difference and are associated
470 with large value of the maximum work W_{max} . Kinetic energy generation exhibits even a
471 higher sensitivity to cycle depth: it is but a small fraction of the maximum work for shallow
472 cycles, but accounts for most of it for the deepest cycle. Both the Gibbs penalty and water
473 lifting also increase with the depth of the cycle, but the sensitivity to the cycle depth is
474 relatively small when compared to either W_{max} or W_{KE} .

475 Figure 7B compares the actual efficiency to the Carnot efficiency for each cycle. Deep
476 cycles not only exhibit a higher Carnot efficiency, but they achieve an actual efficiency close
477 to its theoretical maximum. This indicates that, while the the hydrological cycle acts to
478 greatly reduce the kinetic energy output of shallow convection, it only marginally reduces
479 the output of deep overturning flows such as the inner-core cycle. Finally, Figure 7C shows
480 the temperature of the heat source T_{in} and heat sink T_{out} . This confirms that the increase
481 in efficiency is directly related to the deepening of convection and the decrease in the cooling
482 temperature.

483 Figure 8 shows the evolution of the thermodynamic properties of the deepest MAFALDA
484 cycle through the 15 days of our simulation. This cycle is associated with the value of the

485 isentropic streamfunction equal to 2.5% of its absolute minimum, which corresponds to the
 486 inner-core cycle discussed earlier. The four terms of the kinetic energy budget (10) are shown
 487 in Figure 8A. Both the Gibbs penalty ΔG and water loading terms W_P remain steady. The
 488 intensification on day 5 is however marked by a sharp increase in both the maximum work
 489 W_{max} and kinetic energy generation W_{KE} . This intensification is also evident in the Carnot
 490 efficiency η_C and the actual efficiency of the cycle shown in Figure 8B. The increase in
 491 Carnot efficiency is itself due to the reduction in the cooling temperature (Figure 8C). At
 492 the beginning of the simulation, the cooling temperature is about 260K. It drops sharply
 493 to 240K at day 4, and settles to a value between 230K and 235K for the remainder of the
 494 simulation.

495 5. Conclusion

496 In this paper, we have applied MAFALDA to analyze the thermodynamic transforma-
 497 tions in a high resolution simulation of a hurricane. This technique relies on identifying
 498 the atmospheric overturning by computing a mean circulation in $z - \theta_e$ coordinates, and
 499 extracting a set of thermodynamic cycles that represent the mean overturning flow. This
 500 then allows us to diagnose various thermodynamic transformations that occur through each
 501 cycle.

502 We use MAFALDA here to assess the ability of the hurricane to act as a heat engine.
 503 Previous studies (Pauluis and Held 2002a,b; Pauluis 2016; Laliberte et al. 2015) have demon-
 504 strated that the hydrological cycle has a negative impact on the ability of the atmosphere
 505 to generate kinetic energy. This arises from two key aspects of the hydrological cycle. First,
 506 mechanical work must be performed in order to lift water and is then lost through frictional
 507 dissipation as condensed precipitates (Pauluis et al. 2000). Second, the atmosphere acts
 508 partially as a dehumidifier, in which water is introduced as unsaturated water vapor and re-
 509 moved as a condensate. From a thermodynamic point of view, the water has a lower Gibbs

510 free energy when it enters the atmosphere than when it is removed. This results in a reduc-
511 tion of the amount of work that can be produced by the atmospheric circulation (Pauluis
512 2011). For moist convection, previous studies (Pauluis and Held 2002a; Pauluis 2016) have
513 found that the generation of kinetic energy of moist convection in radiative convective equi-
514 librium is about 10 to 20 percent of the work that could be done by a Carnot cycle acting
515 between the same energy sources and sinks.

516 Here, we contrast two thermodynamic cycles associated with different trajectories in our
517 simulation: a rainband cycle associated with air ascending in the outer rainband located
518 about 200km away from the storm, and a inner-core cycle corresponding to air rising within
519 the eyewall. These two cycles exhibit very different thermodynamic behavior, and, in par-
520 ticular, the generation of kinetic energy for the inner-core cycle is approximately six times
521 larger than for the rainband cycle. We identify three different factors contributing to the
522 high generation rate of the inner-core cycle: (1) an enhancement of the energy transport by
523 the cycle, (2) a very low cooling temperature, characteristic of the upper troposphere, which
524 results in a very high Carnot efficiency, and (3) a relatively small negative contribution from
525 the hydrological cycle, so that the actual efficiency of the inner-core cycle is about two thirds
526 of its Carnot efficiency.

527 The high rate of generation of kinetic energy in the inner-core cycle is strongly tied to
528 the nature of the rising motions within the eyewall. The ascent in the rainband cycle shows
529 a clear indication of entrainment as a gradual decrease of entropy and equivalent potential
530 temperature as the air rises. In contrast, the ascent in the inner-core cycle shows little
531 indication of entrainment of dry air and is almost isentropic. The ascent in the inner-core
532 cycle reaches very high and is associated with very low cooling temperature, which greatly
533 increases the Carnot efficiency. In our simulation, a drop in cooling temperature and a
534 corresponding increase in efficiency precede intensification by about one day. While our
535 work here is limited to a single storm, it strongly suggests that entrainment of dry air into
536 the eyewall, or rather the lack thereof, plays an important role in the intensification and

537 energetics of tropical cyclones.

538 The methodology of MAFALDA is designed to analyze the thermodynamic processes in
539 a numerical simulation. The physical insights it provides should be tempered by the fact
540 that a numerical simulation is at best a good faith effort at reproducing a physical flow. In
541 particular, the horizontal resolution of 2km here is too coarse to fully capture the turbulent
542 nature of entrainment. While we strongly believe that the results presented here are both
543 physically consistent and robust, understanding how numerical resolution and the various
544 physical parameterizations affect the behavior of simulated atmospheric flows remains an
545 important challenge in atmospheric science. Assessing thermodynamic processes represented
546 in such numerical simulations should be an essential component of such endeavor.

547 The novel approach introduced in this study offers a unique perspective on the role played
548 by thermodynamic processes in hurricane formation and intensity. Our study indicates that
549 the atmospheric circulation in a hurricane, characterized by very high generation of kinetic
550 energy, is in a different thermodynamic regime than tropical deep convection. The genesis
551 and intensification of tropical cyclones correspond to the emergence of deep and highly
552 efficient thermodynamic cycles. Systematic applications of MAFALDA should shed further
553 light on how such cycles emerge, and how energy exchanges with both the ocean surface
554 and the surrounding environment can impact the storm intensity and structure, and on how
555 hurricanes and tropical storms behave under different climates.

556 *Acknowledgments.*

557 Olivier Pauluis is supported by the New York University in Abu Dhabi Research Institute
558 under Grant G1102. Fuqing Zhang is partially supported by ONR grant N00014-15-1-2298.
559 The WRF simulation is performed and archived at the Texas Advanced Computing Center.
560 We would like to thank Dandan Tao for running the numerical simulation used in this study.
561 We benefited from discussions with Kerry Emanuel and Juan Fang.

562 A. Appendix: Gibbs relationship for moist air

563 The specific Gibbs free energy is defined as the difference between the specific enthalpy
 564 and the specific entropy multiplied by the absolute temperature:

$$g = h - Ts.$$

565 The specific entropy and specific enthalpy depend on the reference state, and so does the
 566 Gibbs free energy. In this study, we use liquid water at the freezing temperature T_f as the
 567 reference state. The specific enthalpies of water vapor h_v , liquid water, h_l and h_i are

$$h_v = C_l(T - T_f) + L_v \quad (\text{A.1a})$$

$$h_l = C_l(T - T_f) \quad (\text{A.1b})$$

$$h_i = C_i(T - T_f) + L_{f0}. \quad (\text{A.1c})$$

568 Here, C_l and C_i are the specific heat of liquid water and ice, L_v is the latent heat of va-
 569 porization at temperature T , and L_{f0} is the latent heat of fusion taken at the reference
 570 temperature T_f . The corresponding specific entropies s_v , s_l and s_i are

$$s_v = C_l \ln \frac{T}{T_f} + \frac{L_v}{T} - R_v \ln \mathcal{H} \quad (\text{A.2a})$$

$$s_l = C_l \ln \frac{T}{T_f} \quad (\text{A.2b})$$

$$s_i = C_i \ln \frac{T}{T_f} - \frac{L_{f0}}{T_f}, \quad (\text{A.2c})$$

571 with R_v is the specific gas constant for water vapor. For this choice of the reference state,
 572 the specific Gibbs free energy is therefore:

$$g_v = C_l(T - T_f - T \ln \frac{T}{T_f}) + R_v T \ln \mathcal{H} \quad (\text{A.3a})$$

$$g_l = C_l(T - T_f - T \ln \frac{T}{T_f}) \quad (\text{A.3b})$$

$$g_i = C_i(T - T_f - T \ln \frac{T}{T_f}) - L_{f0}(1 - \frac{T}{T_f}). \quad (\text{A.3c})$$

573 We treat here moist air as an ideal mixture of 1 kg of dry air, r_v kg of water vapor, r_l kg
 574 of liquid water and r_i kg of ice. The corresponding entropy and enthalpy *per unit mass of*
 575 *dry air* are

$$s = s_d + r_v s_v + r_l s_l + r_i s_i \quad (\text{A.4})$$

$$h = s_d + r_v h_v + r_l h_l + r_i h_i. \quad (\text{A.5})$$

576 The Gibbs relationship relates the change in entropy to changes in enthalpy, pressure and
 577 composition:

$$Tds = dh - \alpha_d dp - \sum_{w=v,l,i} g_w dr_w. \quad (\text{A.6})$$

578 Here, the specific volume α_d is the specific volume *per unit mass of dry air*:

$$\alpha_d = \frac{R_d T + R_v r_v T}{p}. \quad (\text{A.7})$$

REFERENCES

- 581 Bister, M., and K. A. Emanuel, 1998: Dissipative heating and hurricane intensity. *Meteor.*
582 *Atm. Phys.*, **52**, 233–240.
- 583 Dunion, J. P., 2011: Rewriting the climatology of the tropical north atlantic and caribbean
584 sea atmosphere. *J. Clim.*, **24**, 893–908.
- 585 Emanuel, K. A., 1986: An air-sea interaction theory for tropical cyclones. Part I: Steady
586 maintenance. *J. Atmos. Sci.*, **43**, 585–604.
- 587 Emanuel, K. A., 1994: *Atmospheric Convection*. Oxford University Press, 580 pp.
- 588 Emanuel, K. A., 2003: Tropical Cyclones. *Ann. Rev. Earth. Planet. Sci.*, **31**, 75–104.
- 589 Laliberte, F., J. Zika, L. Mudryk, P. Kushner, J. Kjellsson, and K. Ds, 2015: Constrained
590 work output of the moist atmospheric heat engine in a warming climate. *Science*, **347**,
591 540–543.
- 592 Mrowiec, A. A., O. M. Pauluis, and F. Zhang, 2016: Isentropic analysis of a simu-
593 lated hurricane. *Journal of the Atmospheric Sciences*, **73** (5), 1857–1870, doi:10.1175/
594 JAS-D-15-0063.1, URL <http://dx.doi.org/10.1175/JAS-D-15-0063.1>, [http://dx.doi.org/](http://dx.doi.org/10.1175/JAS-D-15-0063.1)
595 [10.1175/JAS-D-15-0063.1](http://dx.doi.org/10.1175/JAS-D-15-0063.1).
- 596 Pauluis, O., 2011: Water vapor and mechanical work: A comparison of carnot and steam
597 cycles. *J. Atmos. Sci.*, **68**, 91–102.
- 598 Pauluis, O., 2016: The mean air flow as lagrangian dynamics approximation and its appli-
599 cation to moist convection. *J. Atmos. Sci.*, **73**, 4407–4425.

- 600 Pauluis, O., V. Balaji, and I. M. Held, 2000: Frictional dissipation in a precipitating atmo-
601 sphere . *J. Atmos. Sci.*, **57**, 989–994.
- 602 Pauluis, O., and J. Dias, 2013: Satellite estimates of precipitation-induced dissipation in the
603 atmosphere. *Science*, **24**, 953–956.
- 604 Pauluis, O., and I. M. Held, 2002a: Entropy budget of an atmosphere in radiative-convective
605 equilibrium. Part I: Maximum work and frictional dissipation . *J. Atmos. Sci.*, **59**, 125–
606 139.
- 607 Pauluis, O., and I. M. Held, 2002b: Entropy budget of an atmosphere in radiative-convective
608 equilibrium. Part II: Latent heat transport and moist processes . *J. Atmos. Sci.*, **59**, 140–
609 149.
- 610 Pauluis, O., and A. Mrowiec, 2013: Isentropic analysis of convective motions. *J. Atmos. Sci.*,
611 **70**, 3673–3688.
- 612 Rotunno, R., and K. A. Emanuel, 1987: An air-sea interaction theory for tropical cyclones,
613 part ii: Evolutionary study using axisymmetric nonhydrostatic numerical model.
- 614 Skamarock, W. J., and Coauthors, 2008: A description of the advanced research wrf version
615 3. *NCAR Technical Note*.
- 616 Tao, D., and F. Zhang, 2014: Effect of environmental shear, sea-surface temperature and
617 ambient moisture on the formation and predictability of tropical cyclones: an ensemble-
618 mean perspective. *Adv. Model. Earth Syst*, **6**, 384–404.
- 619 Willoughby, H. E., 1999: Hurricane heat engines. *Nature*, **401**, 649–650.
- 620 Zhang, F., and D. Tao, 2013: Effects of vertical wind shear on the predictability of tropical
621 cyclones. *J. Atmos. Sci.*, **70**, 975–983.

622 List of Figures

- 623 1 Schematic representation of a hurricane as a heat engine. Step 1 \rightarrow 2: the
624 low level inflow gains energy from the ocean surface (Q_{in}). Step 2 \rightarrow 3: Air
625 rises from the surface to the upper troposphere, and water condenses and
626 precipitates. Step 3 \rightarrow 1: air is gradually compressed back to the surface and
627 loses energy (Q_{out}) through the emission of infrared radiation. This circulation
628 acts as a heat engine that transports heat from a warm source at temperature
629 T_{in} to a colder sink at temperature T_{out} . This produces mechanical work to
630 generate wind (W_{KE}) and lift condensed water (W_P). The injection of water
631 at the surface and its removal through precipitation are associated with a
632 Gibbs penalty (ΔG) that reduces the kinetic energy output. 30
- 633 2 Minimum pressure (upper panel) and maximum tangential wind (lower panel). 31
- 634 3 Time and azimuthal average of the tangential wind (panel A), equivalent
635 potential temperature (panel B) and stream function (panel C). The solid
636 black line and the dashed blue line correspond to trajectories associated with
637 the inner-core cycle and rainband cycle (see Section 4). On Panel A, three
638 locations have been marked along each trajectory: point 1 is the lowest entropy
639 value, point 2 indicates the highest entropy near the surface, and point 3 is
640 the highest point along the cycle. 32
- 641 4 Isentropic streamfunction in $z - \theta_e$ coordinate. The inner-core cycle (solid
642 black line) and the outer cycle (dashed blue line) correspond to two isolines of
643 the streamfunction. Three locations have been marked along each trajectory:
644 point 1 is the lowest entropy value, point 2 indicates the highest entropy near
645 the surface, and point 3 is the highest point along the cycle. 33

- 646 5 Isentropic averaged value for radius (panel A), tangential wind (panel B),
647 specific moist entropy (panel C), temperature (panel D), mixing ratio (panel
648 E) and Gibbs free energy of water vapor (panel F). The solid black line and
649 the dashed blue line correspond to Eulerian trajectories associated with the
650 inner-core cycle and rainband cycle (see Section 4). 34
- 651 6 The inner-core cycle and rainband cycle are shown in different coordinate
652 pairs: specific moist entropy and temperature (panel A), buoyancy and height
653 (Panel B), total water content and height (panel C), Gibbs free energy of water
654 vapor and mixing ratio (panel D), liquid water content and Gibbs free energy
655 for liquid water (panel E), and ice content and Gibbs free energy for ice (panel
656 F). The inner-core cycle is shown by the solid black line, and the outer cycle
657 by dashed blue line. The trajectories are clockwise in all panels. 35
- 658 7 Thermodynamic analysis for 20 MAFALDA cycles. Panel A: decomposition
659 of the maximum work W_{max} (black) into the generation of kinetic energy
660 W_{KE} (red), water lifting W_P (magenta) and Gibbs penalty ΔG (blue). The
661 inner-core cycle corresponds to cycle 1 and the outer cycle to cycle 8. Panel
662 B: Comparison between the Carnot efficiency η_C (blue) and the effective effi-
663 ciency η (red) for each cycle. Panel C: Temperature of the energy source T_{in}
664 (blue) and energy sink T_{out} (red) for each cycle. 36
- 665 8 Time evolution of the MAFALDA cycle associated 2.5th percentile of the
666 isentropic streamfunction, which corresponds to the inner-core cycle discussed
667 in section 4. Panel A: decomposition of the maximum work W_{max} (black) into
668 the generation of kinetic energy W_{KE} (red), water lifting W_P (magenta) and
669 Gibbs penalty ΔG (blue). Panel B: Comparison between the Carnot efficiency
670 η_C (blue) and effective efficiency η (red). Panel C: Temperatures of the energy
671 sources T_{in} (blue) and of the energy sink T_{out} (red). 37

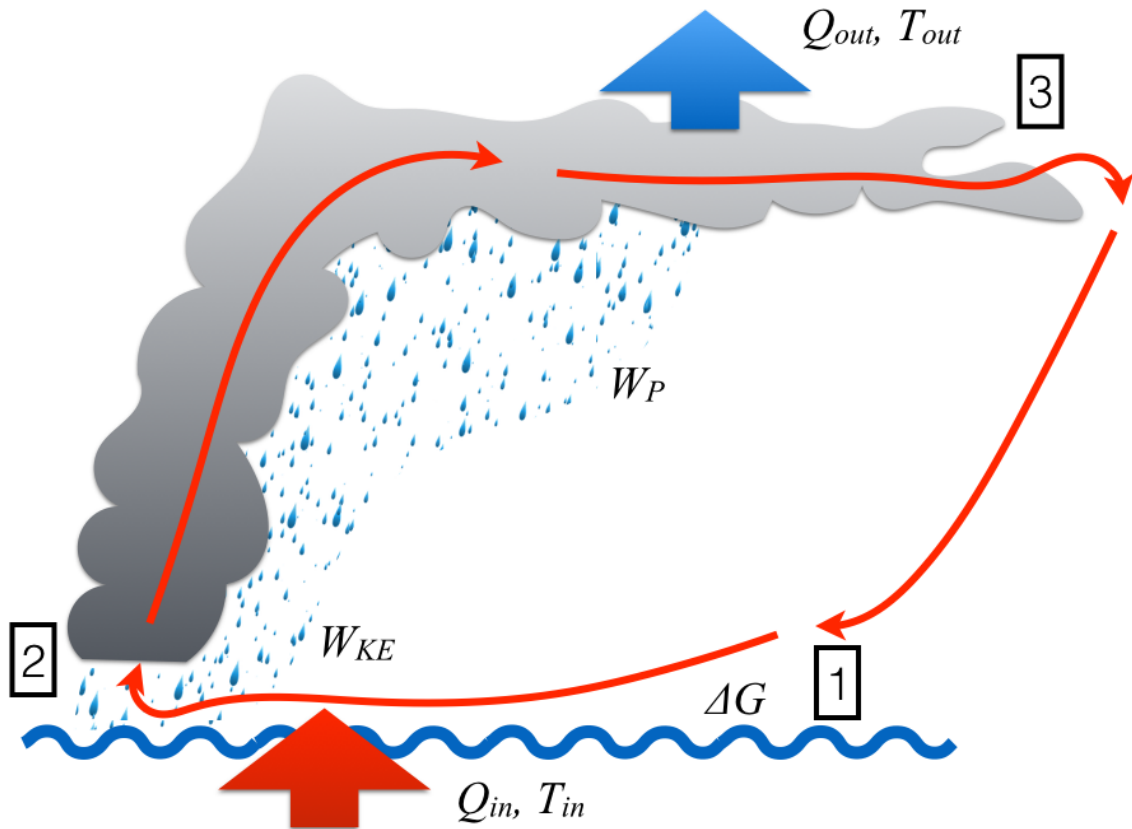


FIG. 1. Schematic representation of a hurricane as a heat engine. Step 1 \rightarrow 2: the low level inflow gains energy from the ocean surface (Q_{in}). Step 2 \rightarrow 3: Air rises from the surface to the upper troposphere, and water condenses and precipitates. Step 3 \rightarrow 1: air is gradually compressed back to the surface and loses energy (Q_{out}) through the emission of infrared radiation. This circulation acts as a heat engine that transports heat from a warm source at temperature T_{in} to a colder sink at temperature T_{out} . This produces mechanical work to generate wind (W_{KE}) and lift condensed water (W_P). The injection of water at the surface and its removal through precipitation are associated with a Gibbs penalty (ΔG) that reduces the kinetic energy output.

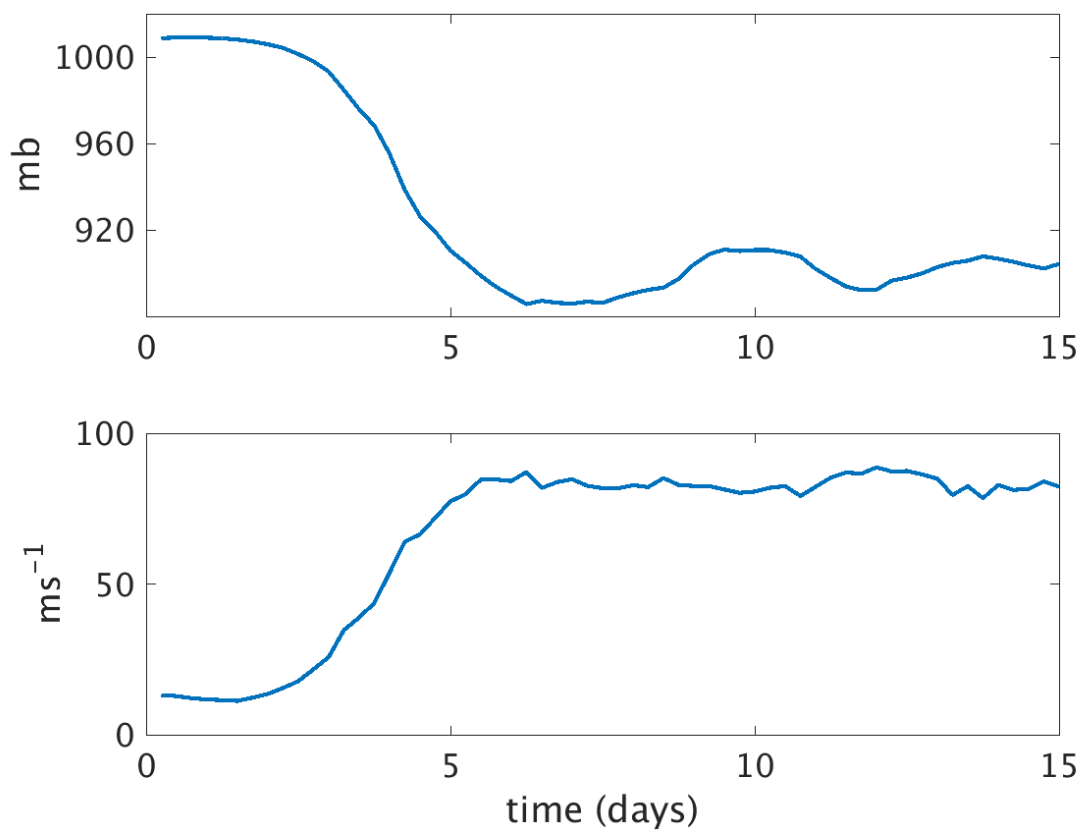


FIG. 2. Minimum pressure (upper panel) and maximum tangential wind (lower panel).

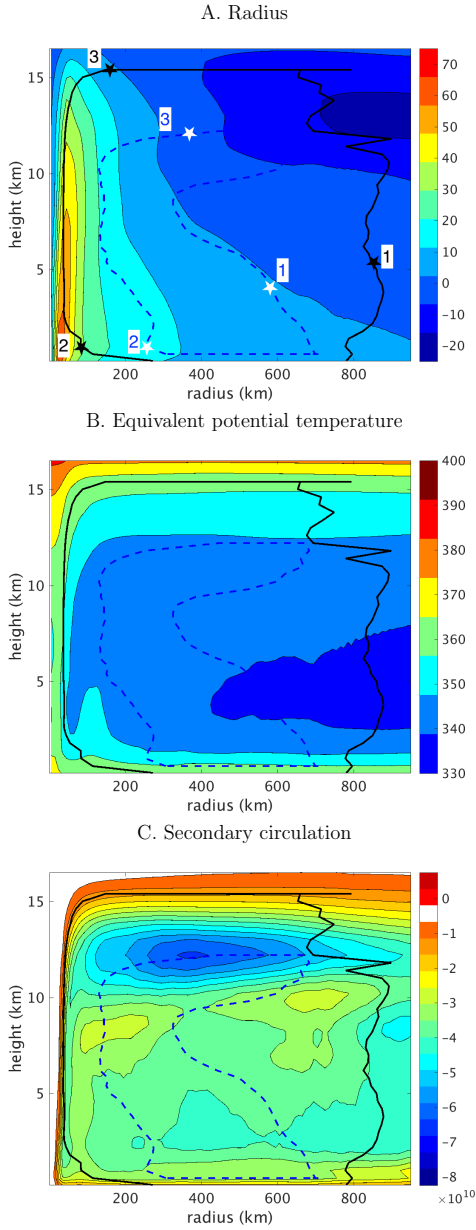


FIG. 3. Time and azimuthal average of the tangential wind (panel A), equivalent potential temperature (panel B) and stream function (panel C). The solid black line and the dashed blue line correspond to trajectories associated with the inner-core cycle and rainband cycle (see Section 4). On Panel A, three locations have been marked along each trajectory: point 1 is the lowest entropy value, point 2 indicates the highest entropy near the surface, and point 3 is the highest point along the cycle.

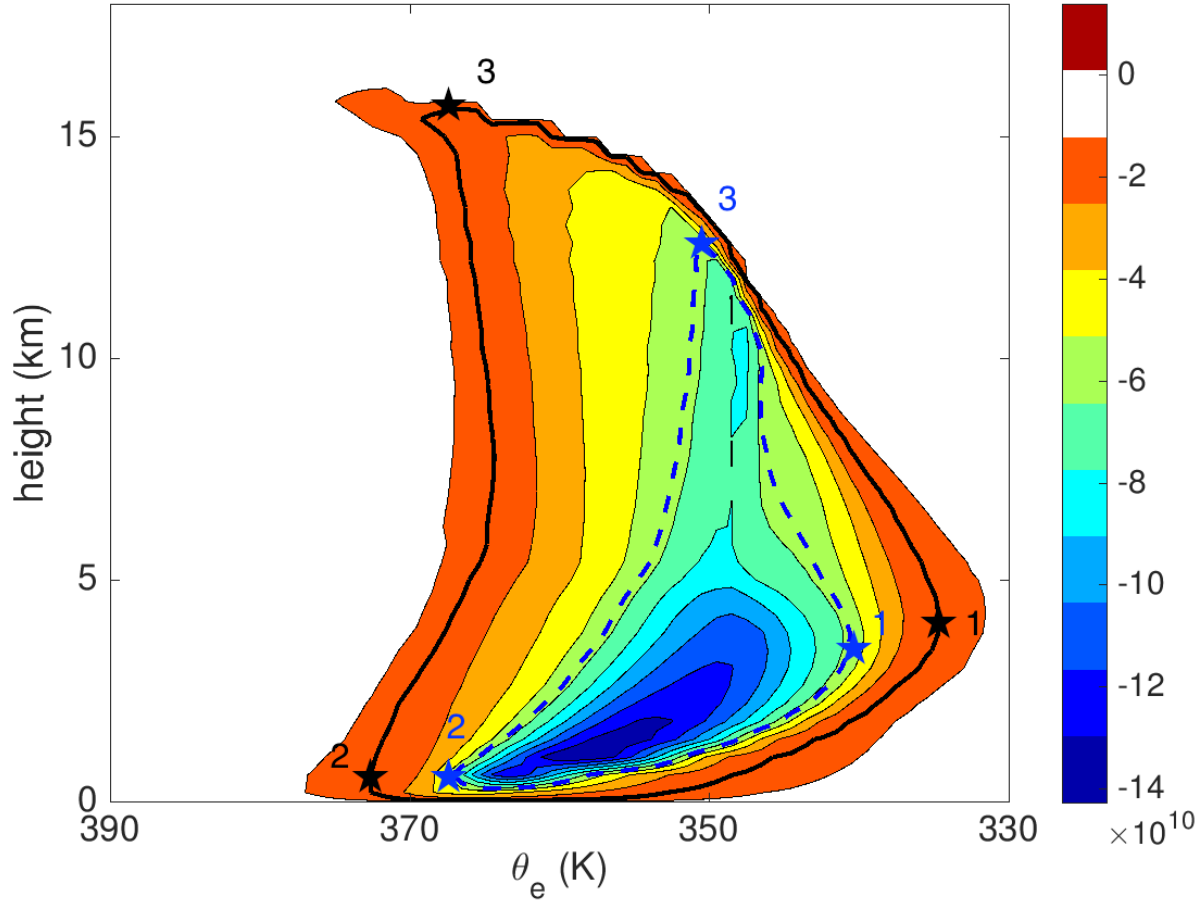


FIG. 4. Isentropic streamfunction in $z - \theta_e$ coordinate. The inner-core cycle (solid black line) and the outer cycle (dashed blue line) correspond to two isolines of the streamfunction. Three locations have been marked along each trajectory: point 1 is the lowest entropy value, point 2 indicates the highest entropy near the surface, and point 3 is the highest point along the cycle.

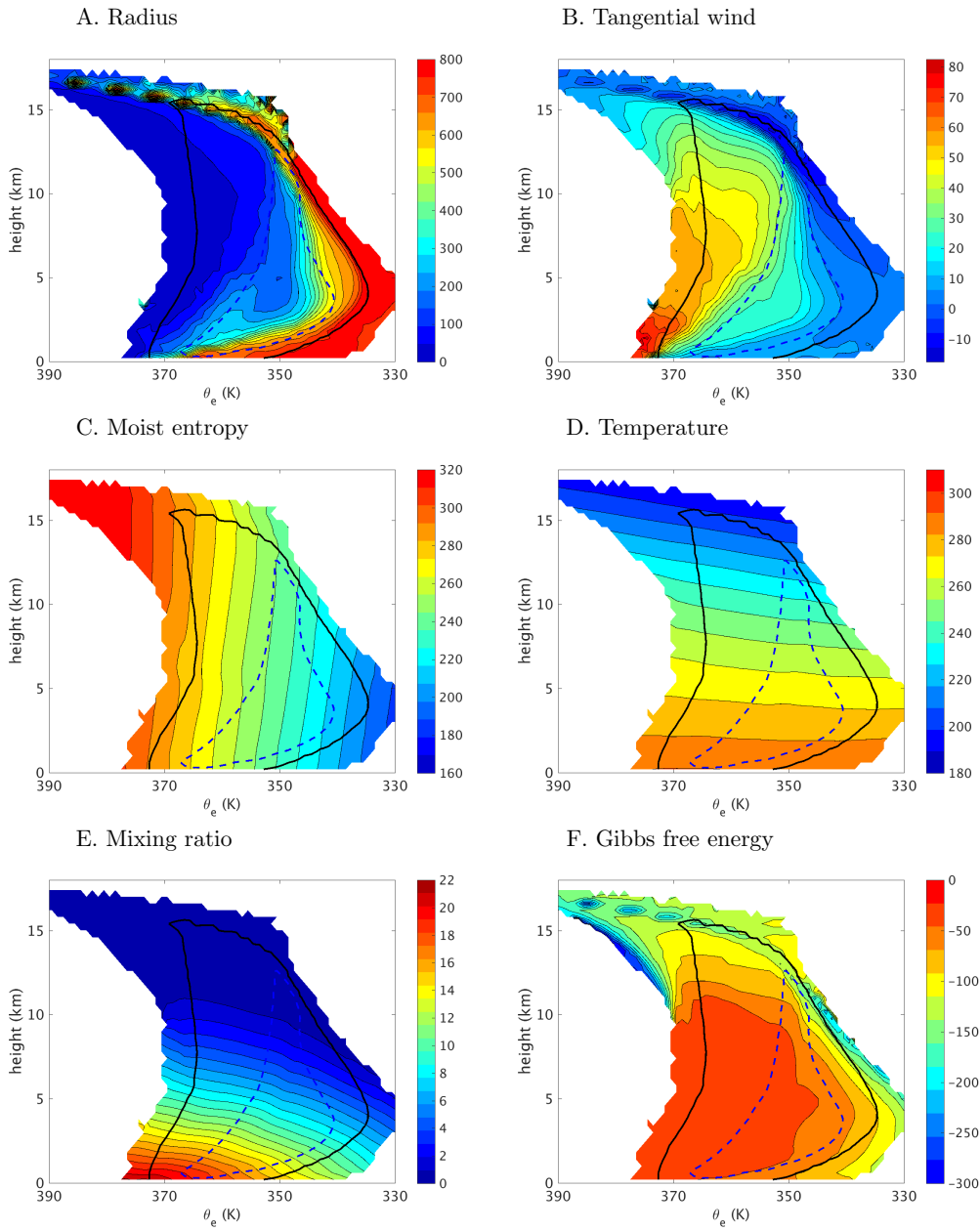


FIG. 5. Isentropic averaged value for radius (panel A), tangential wind (panel B), specific moist entropy (panel C), temperature (panel D), mixing ratio (panel E) and Gibbs free energy of water vapor (panel F). The solid black line and the dashed blue line correspond to Eulerian trajectories associated with the inner-core cycle and rainband cycle (see Section 4).

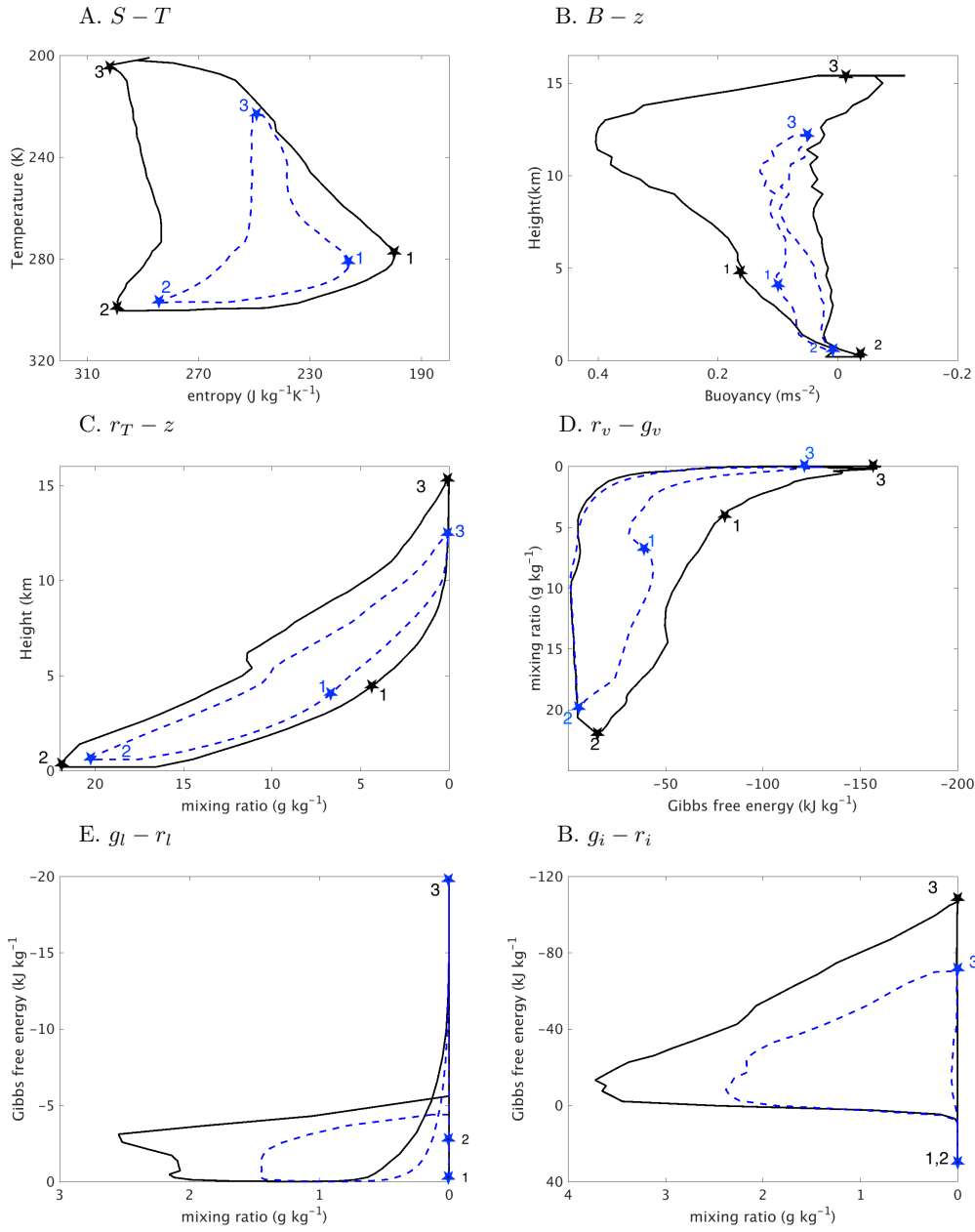


FIG. 6. The inner-core cycle and rainband cycle are shown in different coordinate pairs: specific moist entropy and temperature (panel A), buoyancy and height (Panel B), total water content and height (panel C), Gibbs free energy of water vapor and mixing ratio (panel D), liquid water content and Gibbs free energy for liquid water (panel E), and ice content and Gibbs free energy for ice (panel F). The inner-core cycle is shown by the solid black line, and the outer cycle by dashed blue line. The trajectories are clockwise in all panels.

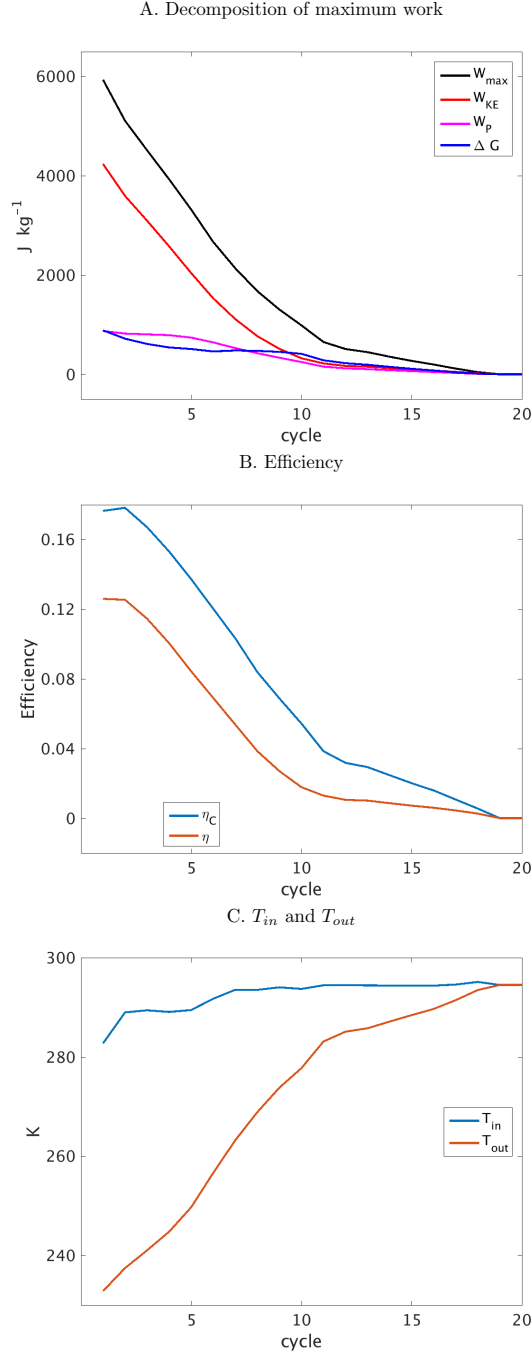


FIG. 7. Thermodynamic analysis for 20 MAFALDA cycles. Panel A: decomposition of the maximum work W_{max} (black) into the generation of kinetic energy W_{KE} (red), water lifting W_P (magenta) and Gibbs penalty ΔG (blue). The inner-core cycle corresponds to cycle 1 and the outer cycle to cycle 8. Panel B: Comparison between the Carnot efficiency η_C (blue) and the effective efficiency η (red) for each cycle. Panel C: Temperature of the energy source T_{in} (blue) and energy sink T_{out} (red) for each cycle.

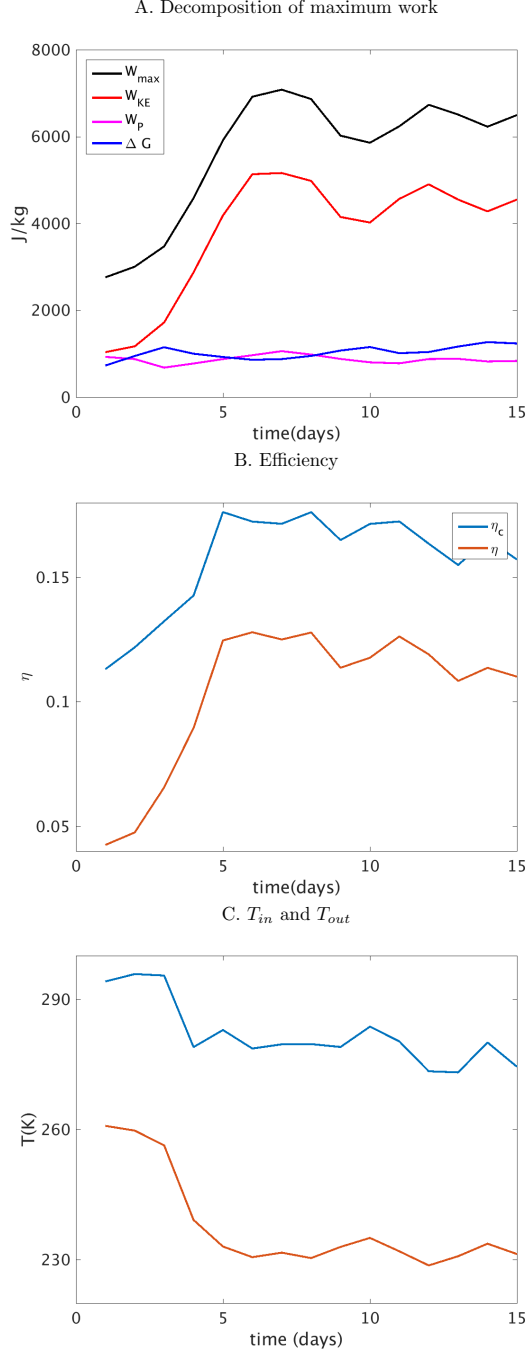


FIG. 8. Time evolution of the MAFALDA cycle associated 2.5th percentile of the isentropic streamfunction, which corresponds to the inner-core cycle discussed in section 4. Panel A: decomposition of the maximum work W_{max} (black) into the generation of kinetic energy W_{KE} (red), water lifting W_P (magenta) and Gibbs penalty ΔG (blue). Panel B: Comparison between the Carnot efficiency η_C (blue) and effective efficiency η (red). Panel C: Temperatures of the energy sources T_{in} (blue) and of the energy sink T_{out} (red).